

Stratospheric Age-of-Air: Sensitivity to Finite-Volume Remapping Algorithm

Clara Orbe^{1,2}, Lawrence L. Takacs^{3,4}, Amal El Akkraoui^{3,4},
Krzysztof Wargan^{3,4}, Andrea Molod³, William Putman³, Steven Pawson³

¹NASA Goddard Institute for Space Studies, New York, NY

²Department of Applied Physics and Applied Mathematics, Columbia University, New York, NY

³Global Modeling and Assimilation Office, NASA Goddard Space Flight Center, Greenbelt, MD

⁴Science Systems and Applications, Inc., Lanham, MD, USA

Key Points:

- The stratospheric mean age-of-air simulated in GEOS is sensitive to the remapping scheme used within the finite-volume dynamical core.
- This sensitivity in the age-of-air is significant ($\sim 30\%$) and imprints on the simulated distributions of several long-lived chemical trace gases, including nitrous oxide and methane.
- The age-of-air sensitivities primarily reflect changes in resolved wave convergence over the Northern Hemisphere midlatitude stratosphere, which impact mean upwelling in the tropical lower stratosphere.

Corresponding author: Clara Orbe, clara.orbe@nasa.gov

18 **Abstract**

19 Accurately modeling the large-scale transport of trace gases and aerosols is critical for interpreting past (and projecting future) changes in atmospheric composition. 20 Simulations of the stratospheric mean age-of-air continue to show persistent biases in chemistry climate models, although the drivers of these biases are not well understood. Here 21 we identify one driver of simulated stratospheric transport differences among various NASA 22 Global Earth Observing System (GEOS) candidate model versions under consideration 23 for the upcoming GEOS Retrospective analysis for the 21st Century (GEOS-R21C). In 24 particular, we show that the simulated age-of-air values are sensitive to the so-called “remap- 25 ping” algorithm used within the finite-volume dynamical core, which controls how in- 26 dividual material surfaces are vertically interpolated back to standard pressure levels af- 27 ter each horizontal advection time step. Differences in the age-of-air resulting from changes 28 within the remapping algorithm approach ~ 1 year over the high latitude middle strato- 29 sphere - or about 30% climatological mean values - and imprint on several trace gases, 30 including methane (CH_4) and nitrous oxide (N_2O). These transport sensitivities reflect, 31 to first order, changes in the strength of tropical upwelling in the lower stratosphere (70- 32 100 hPa) which are driven by changes in resolved wave convergence over northern mid- 33 latitudes as (critical lines of) wave propagation shift in latitude. Our results strongly sup- 34 port continued examination of the role of numerics in contributing to transport biases 35 in composition modeling. 36 37

38 **Plain Language Summary**

39 Large-scale transport plays a crucial role in distributing climatically important trace 40 constituents in the atmosphere, especially in the stratosphere where transport largely 41 determines the chemical lifetimes of trace gases. One summary of transport in the strato- 42 sphere is the “mean age” or the mean transit time since air at a point in the stratosphere 43 was last in the troposphere. Current models used for simulating stratospheric compo- 44 sition produce a range of simulated ages, although these differences are poorly under- 45 stood. Among other factors, model numerics play a critical role in transport, but few 46 studies have explored the sensitivity of the mean age to the choice of numerical scheme 47 employed within different dynamical cores. Here we use one model to show that the mean 48 age is sensitive to the so-called “remapping” algorithm used within the finite-volume dy- 49 namical core that controls how individual material surfaces are vertically interpolated 50 back to standard pressure levels after each horizontal advection time step. This reflects 51 sensitivities in the representation of how waves propagate from the troposphere into the 52 stratosphere. This work suggests that model numerics can be an important factor in con- 53 tributing to differences in simulated transport among models.

54 **1 Introduction**

55 The chemical and radiative properties of the troposphere and lower stratosphere 56 are strongly influenced by the stratosphere-troposphere exchange of mass and tracers (e.g., 57 Morgenstern and Carver (2001); Hegglin et al. (2006); Pan et al. (2007)). Properly sim- 58 ulating the stratospheric circulation and its influence on atmospheric composition in earth 59 system models is important for capturing past decadal trends in surface climate, par- 60 ticularly in response to changes in Southern Hemisphere ozone depletion (e.g., Son et 61 al. (2009); Polvani et al. (2011)). In the Northern Hemisphere (NH), the stratospheric 62 circulation’s coupling to ozone could represent an important feedback on the climate’s 63 response to future increases in greenhouse gases (GHGs), especially over the North At- 64 lantic (e.g., Chiodo and Polvani (2019)). On shorter subseasonal timescales, stratospheric 65 ozone changes associated with strong polar vortex states may also modulate Arctic sea 66 level pressure and surface temperatures (e.g., Ivy et al. (2017); Oehrlein et al. (2020)), 67 so much so that seasonal forecast systems employing prognostic ozone show suggestions

68 of increased signal-to-noise ratio in predictions of the North Atlantic Oscillation (B. M. Monge-
69 Sanz et al. (2022)).

70 Key to accurately simulating a consistent representation of coupling between strato-
71 spheric dynamics and chemical trace gases is ensuring that a model’s underlying trans-
72 port circulation is properly represented. To this end, much effort has been paid to de-
73 veloping and refining so-called “tracer-independent” metrics of transport (Holzer and Hall
74 (2000)) such as the mean age-of-air (Hall and Plumb (1994)) and to applying these mea-
75 sures to rigorously evaluate model transport characteristics in chemistry climate mod-
76 els (CCMs) (e.g., Hall et al. (1999); Orbe et al. (2018); Dietmüller et al. (2018); Aba-
77 los et al. (2020)).

78 While the assessment of CCMs participating in the SPARC Chemistry Climate Model
79 Validation (SPARC CCMVal) effort showed a marked improvement in simulated trans-
80 port characteristics relative to previous intercomparisons (J. Neu et al. (2010)), more re-
81 cent analysis of models participating in the SPARC Chemistry Climate Modeling Ini-
82 tiative (CCMI) (Eyring et al. (2013)) do not demonstrate any improvement (Dietmüller
83 et al. (2018), see their Figure 3). In particular, although some models produce mean age
84 values that agree well with observational estimates, the CCMI intermodel spread is \sim
85 50%, with models generally simulating transport that is too vigorous relative to obser-
86 vations. While documenting these transport differences among models is straightforward,
87 understanding the drivers of this spread remains a key challenge and there is still no con-
88 sensus on what is causing the large spread in simulated ages among the current gener-
89 ation of CCMs.

90 A key challenge in identifying the drivers of age-of-air – and other stratospheric trans-
91 port – biases is that they reflect the time-integrated effects of advection by the residual
92 mean circulation and eddy diffusive mixing, or the quasi-random transport due to the
93 breaking of Rossby waves (e.g., Holton et al. (1995); Plumb (2002)). Given that the in-
94 fluences of mixing and advection are not easily separable, studies have come to differ-
95 ent conclusions about sources of age biases in models. In particular, the analysis of the
96 CCMVal models showed a strong correlation between the intermodel spread in the age-
97 of-air and lower stratospheric tropical upwelling, whereas Dietmüller et al. (2018) showed
98 that the age spread among the CCMI models was driven by differences in mixing. While
99 future attempts to further distinguish between sources of age biases using either simpli-
100 fied “leaky pipe” models (Plumb (1996); J. L. Neu and Plumb (1999)) or more complete
101 measures of the transport circulation such as the “age spectrum” (e.g., Hall and Plumb
102 (1994); Waugh and Hall (2002))) may prove enlightening, at present there is no consen-
103 sus on what is causing large simulated age-of-air biases in models.

104 One potential limitation of previous work based on multi-model intercomparisons
105 is that many aspects of model formulation can influence both stratospheric upwelling and
106 mixing. Thus, while intercomparisons are useful for identifying common model biases,
107 understanding the drivers of these biases is difficult absent single model-based process
108 studies. Among these, several aspects of model formulation have been identified as in-
109 fluencing simulated mean age distributions. As the mean age is sensitive to vertical mo-
110 tion in the lowermost stratosphere, these include large sensitivities to vertical resolution
111 (Orbe et al. (2020)) and to spurious vertical mixing either introduced in vertical coor-
112 dinate transformations in offline chemical transport models (B. Monge-Sanz et al. (2007))
113 or through use of assimilated winds performed either in offline (e.g., Legras et al. (2004))
114 or online data assimilation and “nudged” configurations (e.g., Pawson et al. (2007); Orbe
115 et al. (2017); Davis et al. (2022)). These age sensitivities can be still further amplified,
116 depending on whether or not parameterized gravity waves are included (Eichinger et al.
117 (2020)).

118 By comparison, sensitivities of the mean age to underlying tracer numerics have
119 been less well examined, although Eluszkiewicz et al. (2000) documented a large sensi-

120 tivity in simulated age-of-air values to the choice of advection scheme. More recently,
 121 Gupta et al. (2020) showed differences of $\sim 25\%$ in the age-of-air across identical exper-
 122 iments performed using four different dynamical cores, especially between those using
 123 spectral versus finite-volume schemes. The experiments employed in that study, how-
 124 ever, were highly idealized and it is not clear if the strong influence of tracer numerics
 125 that they identified is also realized in more comprehensive model simulations with moist
 126 physics, especially in the context of model development as carried out in operational mod-
 127 eling centers.

128 To better elucidate this influence of tracer numerics on the transport properties sim-
 129 ulated in a comprehensive global model context, here we document the sensitivity of the
 130 stratospheric mean age in several recent versions of the NASA Global Earth Observing
 131 System (GEOS) general circulation model (Molod et al., 2015) that represent different
 132 stages in model development since the Modern-Era Retrospective Analysis for Research
 133 and Applications Version 2 (MERRA-2; Gelaro et al. (2017)).

134 Our focus on transport evaluation is in wake of the upcoming release of the GEOS
 135 Retrospective analysis for the early 21st Century (GEOS-R21C), which will serve as an
 136 intermediate atmospheric reanalysis between MERRA-2 and the future coupled atmosphere-
 137 ocean reanalysis MERRA-3 (in-preparation). As part of the current effort to explore cou-
 138 pling of more Earth System components targeting MERRA-3, GEOS-R21C will be used
 139 to drive an off-line chemistry reanalysis R21C-Chem with a full chemistry model (GEOS-
 140 Chem) and an advanced Constituent Data Assimilation component to update the chem-
 141 istry fields. Since R21C-Chem will be produced in replay-mode (one-way coupling) whereby
 142 the meteorology fields are used to define the background atmospheric flow (Orbe et al.,
 143 2017), it is imperative that GEOS-R21C produces a credible representation of transport
 144 processes.

145 In particular, here we document how in the process of evaluating candidate sys-
 146 tems for GEOS-R21C we found that the mean age was ~ 1 year younger (or $\sim 30\%$ smaller)
 147 than the values simulated in the model version used to produce MERRA-2 (Figure 1).
 148 The model versions shown in Figure 1 reflect more than 10 years' worth of accumulated
 149 changes in model development, most notably changes in radiation, parameterized con-
 150 vection and, as we focus on here, changes in the model's description of vertical advec-
 151 tion. More precisely, we show that slight modifications to the so-called "remapping" al-
 152 gorithm, which is used to transform advected fields from Lagrangian levels to the new
 153 pressure levels after each horizontal advection time step, are the primary driver of the
 154 age-of-air changes exhibited in recent GEOS-R21C candidate model versions. Thus, whereas
 155 Gupta et al. (2020) highlighted large differences between dynamical cores employing spec-
 156 tral versus finite-volume (FV) numerics, our results show that large transport differences
 157 can occur even within a given FV dynamical core, a result which may have broader im-
 158 plications for other general circulation models employing FV numerics. We begin by dis-
 159 cussing methods in Section 2 and present key results and conclusions in Sections 3 and
 160 4, respectively.

161 2 Methods

162 2.1 Model Configurations

163 Here we present results from several versions of GEOS spanning MERRA-2 to more
 164 recent candidates for GEOS-R21C. Among these model versions, a subset are more "of-
 165 ficial" as they have been documented and/or employed in recent model intercomparisons
 166 and are highlighted in Figure 1. In particular, these include a model version that was
 167 used in Phase 1 of CCM1 and documented in Orbe et al. (2017) (Fig. 1, red line). A more
 168 recent model version that was used in the CCM1 Phase 2 simulations (correspondence
 169 with Michael Manyin) is also shown (Fig. 1, green line).

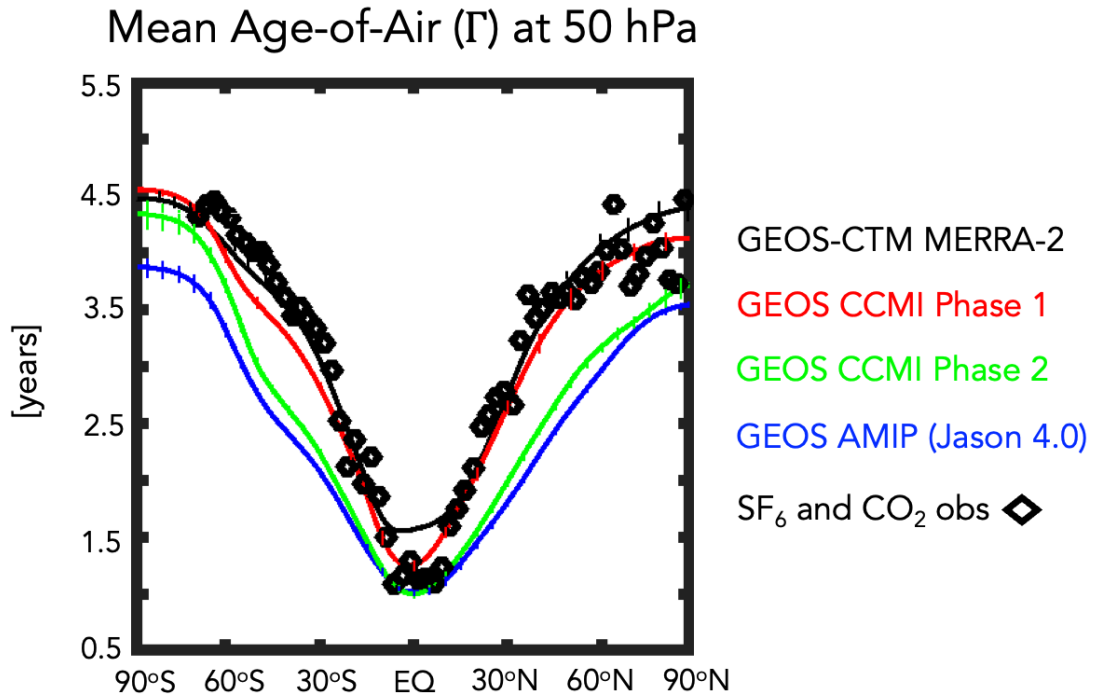


Figure 1. The 2000-2010 climatological annual mean meridional profile of the stratospheric mean age-of-air (Γ), evaluated at 50 hPa. Results from a GEOS-CTM integration constrained with MERRA-2 meteorological fields (black line) as well as free-running GEOS simulations using a model configuration for CCM1 Phase 1 (red line), CCM1 Phase 2 (green line) and a more recent GEOS-FP development tag (Jason 4.0, blue line) are shown. All simulations are constrained with the same (observed) historical sea surface temperatures. Diamonds correspond to SF₆ and CO₂ in situ based estimates of Γ from Boering et al. (1996) and Engel et al. (2009). Vertical dashed lines denote $\pm\sigma$, the standard deviation of Γ over 2000-2010, for each model simulation.

170 We begin by comparing 10-year (2000-2010) climatological mean zonally averaged
 171 age-of-air profiles at 50 hPa across this subset of model versions, derived from 30-year
 172 long atmosphere-only (AMIP) integrations constrained with observed sea surface tem-
 173 peratures (Figure 1). First, we note that the profiles for the CCM1 Phase 1 version of
 174 the model are very close to observations (black stars), consistent with the
 175 “GEOSCCM” documented age characteristics reported in Dietmüller et al. (2018) (see
 176 their Figure 3). In addition, while passive tracers were not integrated within MERRA-
 177 2, results using the GEOS chemistry transport model (GEOS-CTM, Kouatchou et al.
 178 (2015)) constrained with MERRA-2 meteorological fields (black line) also exhibits good
 179 agreement with observed values. This good agreement between the CTM-generated age-
 180 of-air and the observations is consistent with results from a previous GEOS-CTM sim-
 181 ulation (constrained with MERRA) as documented in Orbe et al. (2017).

182 Moving to more recent development versions of the model (green and blue lines),
 183 however, reveals a reduction in the mean age by ~ 1 year over both southern and north-
 184 ern high extratropical latitudes, or a decrease of ~ 20 -30% relative to the MERRA-2 con-
 185 strained simulation and the observations. As discussed earlier, the green line refers to
 186 the CCM1 Phase 2 model version, whereas the blue line refers to an undocumented candi-
 187 date version (model tag Jason 4.0) that corresponds best to a model configuration simi-
 188 lar to what is used in the GEOS forward processing (FP) numerical weather prediction
 189 system. Note that this decrease in the climatological age in both model versions far ex-
 190 ceeds the (internal) variations in mean age that occur interannually (vertical bars on solid
 191 lines).

192 There are numerous development updates in the model that have occurred since
 193 MERRA-2. Therefore, after discussing the model configurations highlighted in Figure
 194 1 in Section 3.1, we then present results from targeted experiments aimed at successively
 195 undoing these changes one-by-one (Section 3.2). Among those aspects most relevant to
 196 the stratospheric transport circulation, we first present results from experiments which
 197 undo recent changes in the radiation scheme, which was updated from Chou and Suarez
 198 (1994) in the shortwave and Chou (1990, 1992) in the longwave to the Rapid Radiative
 199 Transfer Model for GCMS (RRTMG; Iacono et al. (2008)).

200 After addressing the radiation changes, we focus on a still more consequential up-
 201 date that was made in the process of transitioning from the FV dynamical core used in
 202 MERRA-2 (Lin (2004)), hereafter referred to as the GMAO FV core, to the Geophys-
 203 ical Fluid Dynamics Laboratory (GFDL) FV3 dynamical core (Lin et al. (2017)). In par-
 204 ticular, this transition highlighted large sensitivities in the model’s transport properties
 205 to changes in vertical motion, which is realized in the model through the Lagrangian trans-
 206 port of the “floating” vertical coordinate. In particular, after each horizontal advection
 207 step individual material surfaces are vertically interpolated back to the model’s refer-
 208 ence Eulerian coordinate through FV’s so-called “REMAP” algorithm. This remapping
 209 is needed because the Lagrangian surfaces that vertically bound the finite volumes will
 210 eventually deform, negatively impacting the accuracy of the horizontal-to-Lagrangian-
 211 surface transport and the computation of the pressure-gradient terms.

212 The implementation of the remapping algorithm within the GMAO FV core as used
 213 in MERRA-2 is shown in Table 1 and involves 1) fitting piecewise parabolic (hereafter
 214 PPM) functions to input layer-mean values of U , V , Q and tracers; 2) calculating PPM
 215 functions to output layer edges; 3) integrating PPM functions between output layer edges
 216 to produce new layer-mean values of U , V , Q and tracers; 4) calculating total energy (TE)
 217 at input mid-layer pressures; 5) calculating TE at output mid-layer pressures using cu-
 218 bic interpolation and applying an a-posteriori integral conservation; and, finally, 6) remap-
 219 ping temperatures from total energy via $T = (TE - K - \Phi)/C_p$. Here T , U , V , Q , C_p ,
 220 K and Φ correspond to temperature, zonal wind, meridional wind, specific humidity, spe-
 221 cific heat capacity and kinetic and potential energy, respectively.

Table 1. GMAO Core Finite-Volume Remapping Algorithm: The remapping algorithm examined in this study controls how individual material surfaces are vertically interpolated back to standard pressure levels. Employing linear – and to a lesser extent – quadratic interpolation in Step 5 produces stratospheric transport characteristics that are more consistent with the most recent GEOS model configurations (green and blue lines, Figure 1), whereas a cubic interpolation is more consistent with older configurations (red and black lines, Figure 1) and with MERRA-2. Here T , U , V , Q , C_p , K and Φ correspond to temperature, zonal wind, meridional wind, specific humidity, specific heat of air at constant pressure and kinetic and potential energy, respectively.

Step	REMAP Procedure (MERRA-2, GMAO FV Core)
1	Fit PPM functions to input layer-mean U , V , Q and tracers
2	Calculate PPM to output layer edges
3	Integrate PPM functions between output layer edges to produce new layer-mean U , V , Q and tracers
4	Calculate $TE = C_p T + K + \Phi$ at input mid-layer pressures
5	Calculate TE at output mid-layer pressures using cubic interpolation and a-posteriori integral conservation
6	Construct “remapped” T via $T = (TE - K - \Phi)/C_p$

222 As we show in Section 3, much of the degraded skill in the simulated stratospheric
 223 transport that occurred in transitioning to the GFDL FV3 core resembles the degrada-
 224 tion that occurs when using a lower order (linear) interpolation scheme in Step 5 of the
 225 remapping algorithm (Table 1). This otherwise innocuous change in the remapping al-
 226 gorithm in turn highlights the large sensitivities in transport that can occur even *within*
 227 a given finite-volume numerical scheme, in our case resulting in large differences in lower
 228 stratospheric upwelling and a $\sim 30\%$ reduction in the simulated mean age of air.

229 Finally, it is worth noting other important model development changes that occurred,
 230 particularly those related to the parameterization of deep convection (Grell and Freitas
 231 (2014); Freitas et al. (2018)), could directly impact the stratospheric circulation by in-
 232 fluencing wave generation in the troposphere. Although these changes have had a sub-
 233 stantial impact on the diurnal cycle of precipitation (Arnold et al. (2020)) and on con-
 234 vective transport within the troposphere (Freitas et al. (2020)), their influence on the
 235 large-scale stratospheric circulation is much smaller relative to the remapping and ra-
 236 diation changes.

237 2.2 Model Experiments

238 2.2.1 AMIP vs. EMIP

239 We begin our analysis by interpreting the results shown in Figure 1, which are all
 240 based on historical AMIPs that were performed at the same cubed sphere C180 (approx-
 241 imately half-degree) horizontal resolution. As they represent more official model versions
 242 they serve as an important motivation for the experiments that follow. However, there
 243 are numerous (potentially compensating) development changes between these model ver-

244 sions which renders it nearly impossible to cleanly identify drivers of differences in their
 245 simulated transport.

246 To this end, in order to investigate the drivers of the differences in Figure 1 we per-
 247 form targeted modeling experiments aimed at disentangling the influence of individual
 248 model development changes on stratospheric transport properties (Table 2). In order to
 249 evaluate impacts on transport climate statistics, we consider both a set of climatolog-
 250 ical AMIP (rows 1-4) as well as so-called “EMIP” (rows 5-7) experiments.

251 In particular, we carry out 30-year-long AMIP simulations at C180 resolution which
 252 we use to infer the climate characteristics of the different model configurations. The “EMIP”
 253 experiments – ensembles of 3-month-long integrations initialized on approximately Novem-
 254 ber 15 of each year between 1985 and 2015 – are also used to infer impacts on simulated
 255 transport climate. As they are more computationally efficient than AMIPs since all 30
 256 3-month integrations may be run in parallel, they are performed at both C180 and C360
 257 resolutions in order to examine the sensitivity of our results to changes in horizontal res-
 258 olution.

259 As shown in Appendix B, comparisons of the December-January-February (DJF)
 260 vertical profile of tropical upwelling show excellent agreement between EMIP and AMIP
 261 integrations carried out using the same model configuration (Appendix Figure B1). This
 262 somewhat incidental result represents, to the best of our knowledge, the first time that
 263 EMIP-based statistics have been shown to converge well to those from AMIPs for the
 264 stratospheric metrics considered in this study. This suggests that EMIPs, relative to AMIPs,
 265 may be used to provide a computationally more efficient initial assessment of the impacts
 266 of model changes on the stratospheric circulation.

267 *2.2.2 Model Development Changes*

268 Moving next to the precise model development changes examined, we begin by defin-
 269 ing a control experiment (CTRL; Table 2, row 1), which best corresponds to the blue
 270 line shown in Figure 1. Then we define three new AMIP experiments, which aim to dis-
 271 tinguish between the age-of-air changes resulting from changes in radiation versus changes
 272 in the handling of the REMAP algorithm that occurred in the transition from the GMAO
 273 to the FV3 cores (Section 3.2.1).

274 Specifically, these include experiments in which we a) revert back from RRTMG
 275 to the radiation from Chou and Suarez (1994) (CSRAD; Table 2, row 2), b) revert back
 276 from the current FV3 REMAP approach to the settings used within the GMAO FV core
 277 when producing MERRA-2 (i.e., M2REMAP; Table 2, row 3) and c) combine these two
 278 changes (CSRAD+M2REMAP; Table 2, row 4).

279 As we show in Section 3.2.1, the M2REMAP experiment produces the largest changes
 280 in age-of-air, compared to the experiment in which only the radiation is altered. Inter-
 281 preting this result, however, is not straightforward since there are several differences in
 282 the remapping algorithm between the GMAO and FV3 cores. To this end, in order to
 283 simplify the problem we focus the remainder of our investigation (Section 3.2.2) on ex-
 284 amining a clean set of EMIP experiments that are all performed using the GMAO FV
 285 core and that differ from each other only in terms of the order of the interpolation that
 286 is used to calculate TE at the mid-layer pressure levels (Step 5, Table 1). More precisely,
 287 we compare configurations using a linear (LINEAR; Table 2, row 5), quadratic (QUADRATIC;
 288 Table 2, row 6) and cubic interpolation (CUBIC; Table 2, row 7) scheme, with the lat-
 289 ter corresponding to the approach that was used in MERRA-2. To assess the robustness
 290 of our findings to changes in horizontal resolution, all three sensitivity experiments are
 291 run at both C180 and C360 resolutions.

Table 2. GEOS Model Experiments: Targeted GEOS model experiments based off a control experiment (row 1) were carried out to identify the influence of radiation (row 2) and changes in the remapping algorithm used since MERRA-2 (row 3), as well as their combined influence (row 4). The influence of the remapping algorithm changes is then interpreted using a simpler set of sensitivity experiments, performed using the GMAO FV core, in which only the order of the interpolation scheme used to calculate TE at output mid-layer pressure levels is altered (rows 5-7). Experiments in rows 1-4 are 30-year-long AMIPs run at C180 resolution, whereas rows 5-7 refer to 30-member 3-month-long (DJF) EMIP experiments. Both AMIPs and EMIPs are used for climate statistic evaluation (see Appendix A for more on the correspondence between the two). EMIP experiments are run at both C180 and C360 horizontal resolutions.

Experiment Name	Configuration	Experiment Type	Hor. Resolution
CTRL	Control, FV3 Core	AMIP (30 yrs.)	C180
CSRAD	Chou-Suarez (1994) Radiation (RAD)	AMIP (30 yrs.)	C180
M2REMAP	GMAO FV Core (cubic)	AMIP (30 yrs.)	C180
CSRAD+M2REMAP	Chou-Suarez (1994) RAD GMAO FV Core (cubic)	AMIP (30 yrs.)	C180
LINEAR	GMAO FV Core (linear)	EMIP (30 mem.)	C180, C360
QUADRATIC	GMAO FV Core (quadratic)	EMIP (30 mem.)	C180, C360
CUBIC	GMAO FV Core (cubic)	EMIP (30 mem.)	C180, C360

292 These three numerical schemes are derived from the generic interpolation equation:

$$293 \quad \mathcal{Q}(\mathcal{P}) = \sum_{k'} a_{k+k'} \mathcal{Q}_{k+k'} \quad k' = 0, \pm 1, \pm 2, \dots \quad (1)$$

294 where \mathcal{P} represents the target output location in $\ln(p)$ and $\mathcal{Q}_{k+k'}$ denotes the surround-
295 ing grid-point values at input locations. The coefficients $a_{k+k'}$ are derived through Tay-
lor Series expansions using non-uniform grid spacing given by:

$$a_{k+k'} = \frac{\prod_m (\mathcal{P}_{k+m} - \mathcal{P})}{\prod_m (\mathcal{P}_{k+m} - \mathcal{P}_{k+k'})} \quad m = 0, \pm 1, \pm 2, \dots \quad m \neq k' \quad (2)$$

296 For the three schemes, the grid points used are: LINEAR ($k, k-1$), QUADRATIC ($k+$
297 $1, k, k-1$), and CUBIC ($k+1, k, k-1, k-2$). In all cases, the grid points are chosen
298 such that the target location resides between layers k and $k-1$.

299 Note that, while the LINEAR and QUADRATIC experiments do not actually cor-
300 respond to any of the model versions shown in Figure 1, they highlight the large sensi-
301 tivity of the mean age to changes in the interpolation scheme that may otherwise seem
302 innocuous. They also provide further evidence of the strong influence of changes in tropi-
303 cal lower stratospheric upwelling strength on the stratospheric mean age in GEOS.

304 Finally, in all experiments using the MERRA-2 remapping approach (i.e., M2REMAP,
305 CSRAD+M2REMAP, LINEAR, QUADRATIC, CUBIC) additional modifications to the
306 divergence damping coefficients were used so as to best ensure consistency with what was
307 used in MERRA-2. Specifically, these include changes to the number of layers for ver-
308 tical subgrid mixing, the coefficient for barotropic mode damping, the use of 2nd vs. 6th
309 order divergence damping and the strength of the divergence damping coefficients.

310 2.3 Analysis Approach

311 2.3.1 Transport Diagnostics

312 To diagnose the transport circulation we focus primarily on the age-of-air (Hall and
 313 Plumb (1994)). This is inferred from an idealized global “clock” or ideal age tracer (Γ)
 314 (Thiele and Sarmiento (1990)) that is defined with respect to the bottom model level
 315 as follows: initially, the ideal age tracer is set to zero throughout the troposphere and
 316 thereafter held to zero over the entire Earth’s surface, subject to a constant aging of 1
 317 year/year throughout the atmosphere. We present here the statistically stationary (equi-
 318 librated) value of $\Gamma(r)$, which is equal to the average time since the air at a location r
 319 in the stratosphere last contacted the Earth’s surface. In addition to the mean age, we
 320 also show results from an idealized e90 tracer that is uniformly emitted over the entire
 321 surface layer and decays exponentially at a rate of 90 days^{-1} such that concentrations
 322 greater than 125 ppb and less than 50 ppb tend to reside in the lower troposphere and
 323 stratosphere, respectively (Prather et al. (2011)). As this tracer features strong near-
 324 tropopause gradients and takes significantly less time to equilibrate, compared to the mean
 325 age, it is useful for evaluating stratosphere-troposphere-exchange and transport within
 326 the upper troposphere/lower stratosphere (Abalos et al. (2017, 2020); Orbe et al. (2020)).

327 Both the mean age and e90 tracers were integrated in all of the AMIP experiments
 328 shown in Figure 1 and listed in Table 2 (rows 1-4), which were run using the same ide-
 329 alized passive tracer package described in Orbe et al. (2017). Note that the mean age
 330 tracer was not integrated in the EMIP experiments given its much longer characteris-
 331 tic timescale in the stratosphere ($\sim 3\text{-}5$ years). As such, the EMIP simulations, which
 332 do not exceed one year, are not appropriate for evaluating the time-integrated transport
 333 characteristics reflected in the age-of-air.

334 In addition to carrying the idealized tracers, two of the experiments shown in Fig-
 335 ure 1 were also run with full interactive chemistry and correspond to the two CCMI (Phase
 336 1 and Phase 2) integrations (red and green lines, Figure 1). Both simulations employ the
 337 same Global Modeling Initiative (GMI) chemical mechanism (Strahan et al. (2013)) and
 338 are therefore useful in evaluating the impact of age differences on real trace gas distri-
 339 butions. In particular, as shown in Section 3.1 results from these experiments show sig-
 340 nificant imprints of the age-of-air changes on nitrous oxide (N_2O) and methane (CH_4).

341 2.3.2 Circulation Diagnostics

342 As we show in Section 3, the changes in age-of-air across the different model ver-
 343 sions are strongly tethered to changes in the advective component of the circulation, which
 344 we quantify using the Transformed Eulerian Mean (TEM) estimate of the Lagrangian
 345 transport of mass by the circulation. Thus, in addition to more standard Eulerian met-
 346 rics of the circulation (e.g., zonal winds and temperatures), we focus on the vertical com-
 347 ponent of the TEM residual velocity, defined as $\bar{w}^* = \bar{w} + \frac{\partial(\psi \cos\phi)}{\partial\phi}$, where $\psi = \overline{v'\theta'}/\frac{\partial\theta}{\partial p}$
 348 is the eddy stream function, θ refers to potential temperature, a is the Earth’s radius
 349 and overbars and primes denote zonal means and deviations therefrom, respectively (Andrews
 350 et al. (1987)). In addition, we interpret the behavior in w^* using the Eliassen-Palm flux
 351 divergence ($\nabla \cdot \mathbf{F}$), whose horizontal ($\mathbf{F}(\phi)$) and vertical ($\mathbf{F}(p)$) components are respec-
 352 tively defined as $\mathbf{F}(\phi) = \text{acos}\phi[\frac{\partial u}{\partial p}\psi - \overline{u'v'}]$ and $\mathbf{F}(p) = \text{acos}\phi([f - \frac{\partial \overline{u'v'}}{\partial\phi}]\psi - \overline{u'\omega'})$.

353 2.4 Observations and Reanalyses

354 While our focus is on interpreting and understanding the different model config-
 355 urations, we incorporate observations to provide context when possible, although we do
 356 not present an exhaustive evaluation of the model’s transport characteristics (for that
 357 see earlier studies including Orbe et al. (2017, 2018)). However, as the tracers are not

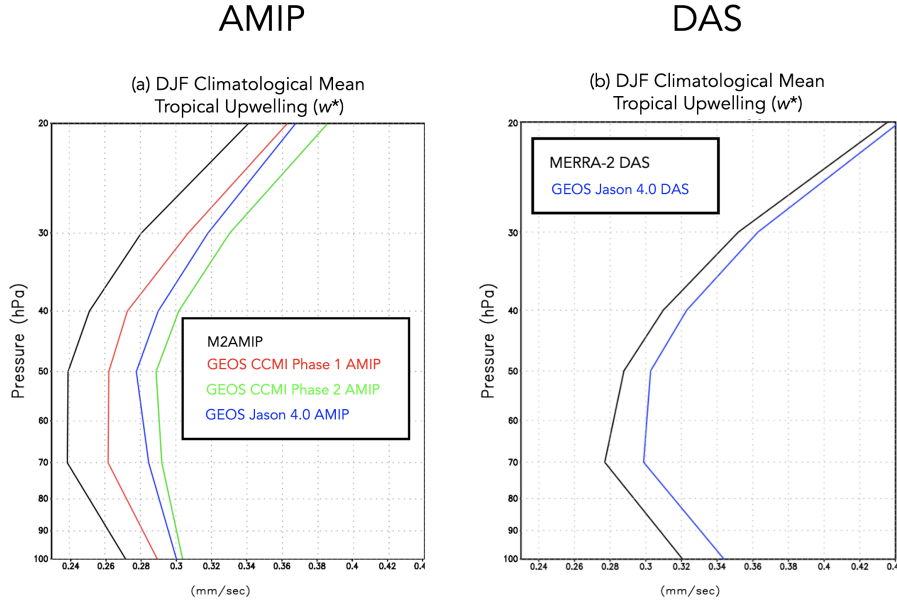


Figure 2. Left: The DJF climatological mean vertical residual mean velocity, w^* , averaged between the turnaround latitudes for GEOS free-running AMIP simulations using the model configurations corresponding to the CCM1 Phase 1 (red) and Phase 2 (green) submissions and to Jason 4.0 (blue). M2AMIP is shown in black. Right: The DJF climatological mean vertical residual mean velocity, w^* , averaged between the turnaround latitudes for MERRA-2 (black) and a data-assimilation configuration of Jason 4.0 (blue). Note that the right panel only uses limited data from years 1997-2021 for which the Jason 4.0 DAS output was available. As they reflect more recent years, the MERRA-2 DAS values in the right panel are therefore larger than the values shown in Figure A1b, given that w^* has increased over more recent decades (see Figure 5.14 in (Fujiwara et al., 2022)).

358 directly integrated in MERRA-2 (with the exception of ozone), we compare against in-
 359 dependent observational estimates. For the mean age we first compare simulated merid-
 360 ional age profiles at 50 hPa with values derived from in situ aircraft measurements of car-
 361 bon dioxide (CO_2), averaged in 2.5 degree latitude bins over the altitude range 19.5 to
 362 21.5 km (Boering et al. (1996), see also Figure 5 in Hall et al. (1999)).

363 We also briefly evaluate impacts of transport biases on the simulated trace gas dis-
 364 tributions for the CCM1 Phase 1 and 2 experiments. The simulated fields of methane
 365 (CH_4) are compared with the climatologies derived for 1991–2002 from the Halogen Oc-
 366 culation Experiment (HALOE) on board the Upper Atmosphere Research Satellite (UARS)
 367 (Groß and Russell III (2005)). Comparisons of simulated nitrous oxide (N_2O) are made
 368 against climatologies derived from the Microwave Limb Sounder (MLS) on the Earth Ob-
 369 serving System (EOS) Aura satellite. Climatologies over the same period (2005–2015)
 370 are used to evaluate both the model and the observations. We use the 190-GHz retrieval
 371 from Version 4.2 because the 640-GHz data set ends in summer 2013 due to the failure
 372 of the N_2O primary band.

373 For the circulation diagnostics nearly all comparisons are made relative to the MERRA-
 374 2 data assimilation (DAS) reanalysis product, noting that comparisons against ERA-5
 375 (not shown) reveal a similar picture. One exception, however, is the vertical component

of the TEM circulation (w^*), which shows some differences in vertical structure between MERRA-2 and a 30-member ensemble of (free-running) AMIP integrations produced using the MERRA-2 model, hereafter referred to as M2AMIP (Collow et al., 2017) (Appendix Figure A1, right). As the free-running model results shown in Figure 1 show more consistency with the vertical profile of M2AMIP, not MERRA-2, we compare w^* in all free-running GEOS experiments with M2AMIP, noting that for non-derived measures (i.e., winds, temperatures), the raw MERRA-2 output is used.

The differences in w^* between M2AMIP and MERRA-2 may reflect the influence of temperature increments in the DAS (MERRA-2) which can drive spurious vertical transport in assimilated products (Weaver et al., 1993; Orbe et al., 2017). In particular, Weaver et al. (1993) showed that the imbalance between the thermal and velocity fields at the time an observation is ingested during the assimilation cycle can excite unwanted inertial-gravity wave modes that manifest strongly in the residual vertical winds. This impact of the increments may therefore explain the differences in w^* , particularly above 30 hPa, where the contribution of temperature increments to the analysis is large. We emphasize, however, that our main interest in this study is on upwelling within the lower stratosphere (i.e., 70-100 hPa), where M2AMIP and MERRA-2 agree well, as this region best correlates with the global age-of-air characteristics. As such, we reserve further exploration of the w^* differences above 50 hPa for future work.

3 Results

3.1 Reduction of Stratospheric Mean Age in GEOS Models Since MERRA-2

We begin by interpreting the reduction in mean age exhibited in more recent model versions in terms of changes in the strength of upwelling in the tropical lower stratosphere. In particular, the reductions in Γ (Figure 1) are consistent with increases in the strength of lower stratospheric tropical upwelling, with w^* becoming progressively stronger in more recent model versions, relative to MERRA-2 (Figure 2a). Note that, while the increases in w^* occur throughout the stratosphere, we focus on the changes occurring between 70 and 100 hPa as these are most relevant to determining the tropical upward mass flux and associated strength of the mean overturning circulation.

Interestingly, the increases in w^* relative to MERRA-2 are not only manifest in 30-year-long AMIPs (Fig. 2a), but also in a DAS configuration of the Jason 4.0 model tag (Fig. 2b), evaluated over a more recent period spanning 1997 to 2021. Though not the main focus of this study, this impact on the DAS simulations has important implications for the development of R21C as it highlights that the assimilation of observations may reduce, but not entirely correct for, the model transport biases that have been introduced in more recent GEOS model versions.

Though perhaps naive, the relationship between lower stratospheric upwelling and the mean age suggested by comparing Figure 1 and Figure 2a is consistent with the long-term behavior of Γ inferred from both historical and projected future climate simulations (Butchart et al. (2010); Abalos et al. (2021)). A strong relationship between the strength of lower stratospheric ascent and the mean age was also shown to hold in the CCMVal models (see Fig. 5.20 in J. Neu et al. (2010)). Nevertheless, it is important to note that a clear relationship between w^* and Γ is not a priori expected, as the age-of-air is also known to be very sensitive to mixing, which may be important in interpreting differences among the CCM1 Phase 1 models (Dietmüller et al. (2018)).

The differences in w^* highlighted in Figure 2 are associated with enhanced Eliassen-Palm flux convergence over NH midlatitudes (Figure 3). Increased wave convergence is evident not only within the subtropical lower stratosphere ($< 30^\circ\text{N}$, 50-100 hPa) but also over higher latitudes and altitudes ($\sim 40^\circ\text{-}70^\circ\text{N}$, 20-50 hPa). The fact that differences

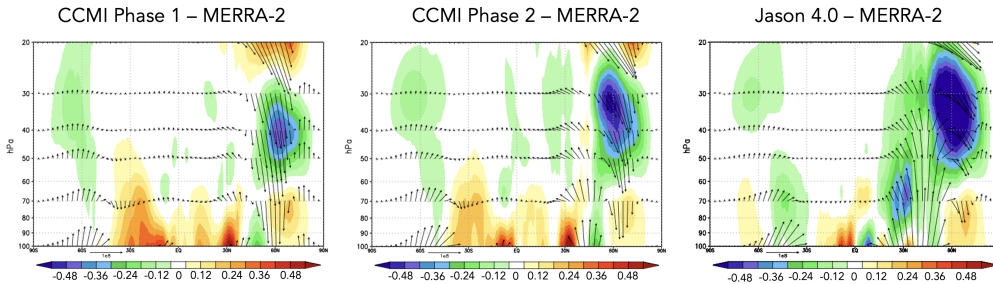
DJF Climatological Mean Eliassen-Palm Flux Divergence ($\nabla \cdot \mathbf{F}$)

Figure 3. Colors show anomalies in the DJF climatological mean Eliassen-Palm (EP) flux divergence between the CCMI Phase 1 (left), CCMI Phase 2 (middle) and Jason 4.0 GEOS AMIP (right) model versions, relative to MERRA-2. Arrows denote anomalies in the vertical and meridional EP flux vectors (relative to MERRA-2).

426 in extratropical wave convergence imprint on tropical upwelling is consistent with our
 427 understanding of the so-called “downward control” principle (Haynes et al. (1991)).

428 In particular, the strength of the residual mean streamfunction (Ψ^*) is, via down-
 429 ward control, directly related to the vertically integrated eddy-induced total zonal force
 430 above that level and has contributions both from the (resolved wave) Eliassen-Palm flux
 431 divergence (Figure 3) as well as the gravity wave drag scheme’s parameterized waves (not
 432 shown). The tropical upward mass flux – defined as $\Psi_{\max}^* - \Psi_{\min}^*$ evaluated at the turnaround
 433 latitudes (e.g. Rosenlof (1995)) – is therefore directly dependent on the wave forcing aloft.

434 One subtlety to note is that the wave convergence changes shown in Figure 3 oc-
 435 cur at high latitudes and are directly associated with downwelling over the polar region.
 436 It is then via mass balance that anomalously strong downwelling associated with enhanced
 437 flux convergences must be accompanied by enhanced upwelling in the tropics. This in-
 438 direct impact of higher latitude wave drag reflects an “extratropical pumping” mecha-
 439 nism (Holton et al., 1995), which is illustrated more clearly in Section 3.2.2 in the con-
 440 text of the LINEAR, QUADRATIC and CUBIC experiments.

441 While the reduction in Γ (Figure 1) of $\sim 30\%$ at 50 hPa is significant, it is neither
 442 clear if this change is representative of other altitudes within the stratosphere nor how
 443 this age bias imprints on real chemical species. To this end, we begin by comparing the
 444 full latitude-pressure distribution of changes in Γ and another passive tracer (e90) (Fig-
 445 ure 4) between the CCMI Phase 1 and Phase 2 model configurations (red and green lines,
 446 Figure 1). In particular, we find that the changes in both passive tracers – large reduc-
 447 tions in Γ within both hemispheres (Fig. 4, top right) and increased values of e90 within
 448 the lower stratosphere (Fig. 4, bottom right) – are reflective of an overall increase in the
 449 strength of the transport circulation. This is highlighted in the CCMI Phase 2 – 1 model
 450 differences for the passive tracer distributions (Fig. 4, right panels) which are shown in
 451 the absence of robust observational constraints of Γ at higher altitudes (or any obser-
 452 vational constraints for e90, for that matter). The reduced/increased stratospheric bur-
 453 dens of the age and e90 tracers are consistent with stronger upwelling in the CCMI Phase
 454 2 model configuration (Figure 2).

455 While the observational constraints on Γ presented in Figure 1 and the departure
 456 of w^* away from MERRA-2 suggest that transport properties of the newer model con-
 457 figurations are moving in the wrong direction, it is relevant to ask whether or not the

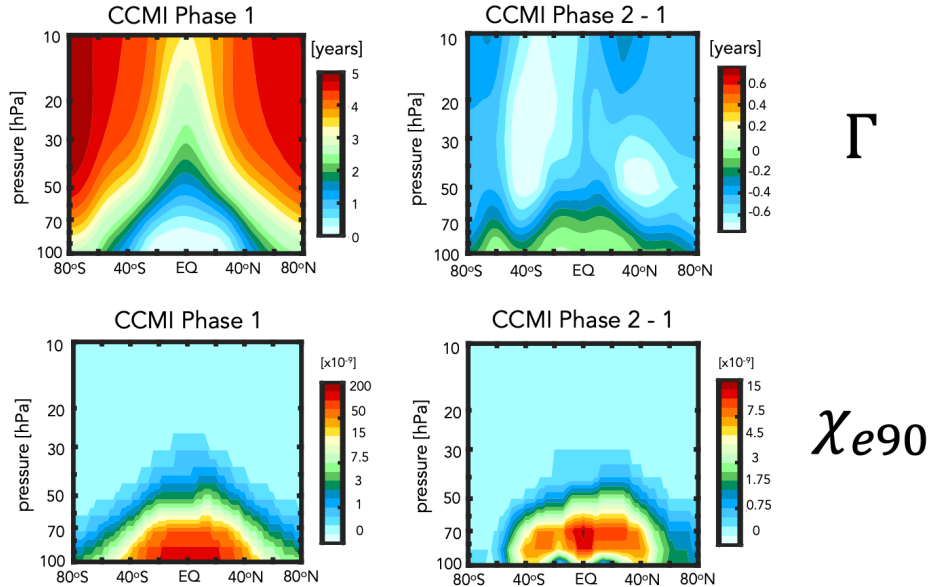


Figure 4. The climatological mean (2000-2010) distribution of the mean age-of-air (Γ) (left, top) and e90 idealized tracers (left, bottom) for the CCMI Phase 1 model configuration. Climatological differences between the CCMI Phase 2 and Phase 1 model configurations are shown in the right panels. Note that a nonlinear colorbar has been used in the e90 subplots.

458 trace gas satellite measurements also support this conclusion. Indeed, comparisons with
 459 observations show larger biases in N_2O (Fig. 5, top panels) and CH_4 (Fig. 5, bottom pan-
 460 els), increasing from 10% to 30% in the CCMI Phase 2 model configuration, depending
 461 on the species. The patterns of these biases are generally consistent with the biases in
 462 the mean age (Fig. 4), suggesting a strong link between the tracers. Recall that the same
 463 chemistry mechanism is used in both CCMI Phase 1 and 2 simulations.

464 The fact that the mean age changes have a significant imprint on the simulated trace
 465 gases is consequential for the GEOS-R21C system. However, the configurations shown
 466 in Fig. 1-5 differ in many respects (physics, resolution, radiation, FV remapping algo-
 467 rithm) and it is difficult to meaningfully interpret what is driving the changes in w^* (and
 468 the tracers). We therefore move next to the targeted model experiments (Table 2) in or-
 469 der to interpret the model development steps that resulted in these transport circula-
 470 tion changes.

471 **3.2 Identifying Drivers of Upwelling and Tracer Changes Since** 472 **MERRA-2**

473 **3.2.1 Radiation versus REMAP Algorithm**

474 As discussed in Section 2, among the model changes that were made since MERRA-
 475 2, the changes in radiation and the FV remapping algorithm are most likely to directly
 476 have impacted the stratospheric circulation. We therefore begin by assessing which of
 477 these changes dominates the decreases in Γ shown in Figure 1.

478 Figure 6 shows the distribution of Γ for experiments in which the longwave, short-
 479 wave, and REMAP updates since MERRA-2 have successively been undone. Relative

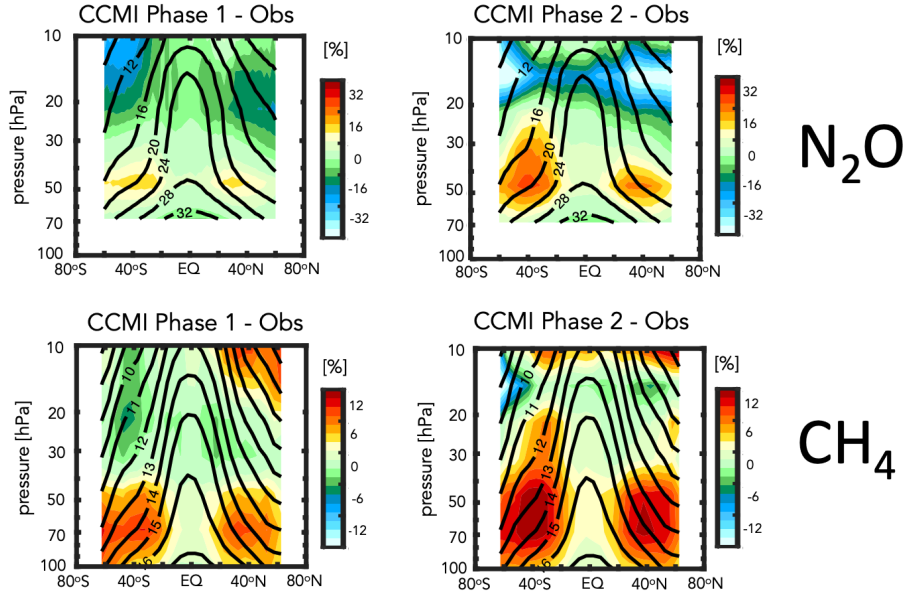


Figure 5. Colors shown anomalies in the simulated distributions of nitrous oxide (N_2O) (top) and methane (CH_4) (bottom), relative to the MLS and HALOE observed values, respectively, for the CCMI Phase 1 (left) and Phase 2 (right) GEOS model configurations. Climatological mean observed values are shown in the black contours.

480 to the control experiment (CTRL; Table 2, row 1), the reversion back to Chou and Suarez
 481 (1994) in the shortwave and Chou (1990, 1992) in the longwave results in an increase in
 482 the mean age of ~ 0.5 years throughout the stratosphere (CSRAD; Table 2, row 2). Though
 483 significant, this change in Γ is smaller than the change that results from reverting back
 484 to the remapping approach used in MERRA-2 (M2REMAP; Table 1; row 3), in which
 485 the mean age increases by ~ 1 year. The combined impacts of both changes (CSRAD+M2REMAP;
 486 Table 1 row 4) is roughly linear, with age values of ~ 5.5 years over high latitudes at 50
 487 hPa, consistent with the values simulated by the GEOS-CTM MERRA-2 integration (black
 488 line, Figure 1) and with the CCMI Phase-1 version of the model (red line, Figure 1).

489 Next we ask if the behavior of Γ exhibited in Figure 6 can be interpreted in terms
 490 of changes in the strength of lower stratospheric tropical upwelling and extratropical wave
 491 convergence, as our previous analysis of the CCMI experiments suggested. Indeed, Figure
 492 7 shows that values of upwelling decrease in the CSRAD and M2REMAP experiments,
 493 relative to the CTRL integration. The increase in upwelling resulting from both changes
 494 (CSRAD+M2REMAP) is still larger, consistent with the larger age decreases in that ex-
 495 periment. This change in the behavior of w^* within the tropical stratosphere can be in-
 496 terpreted in terms of changes in the Eliassen Palm flux convergence over NH midlati-
 497 tudes (not shown), which features smaller values in the CSRAD, M2REMAP (and CSRAD+
 498 MSREMAP) experiments. Note that our examination of the changes in w^* are derived
 499 from EMIP integrations, which we showed previously converge (for DJF) to the statis-
 500 tics derived from corresponding AMIP experiments.

501 3.2.2 FV REMAP Algorithm: Sensitivity of Climate Statistics

502 Having shown in the previous section that the largest changes in the mean age were
 503 realized through the differences in remapping approaches between the GMAO FV core

Annual Climatological Mean Stratospheric Mean Age (Γ)

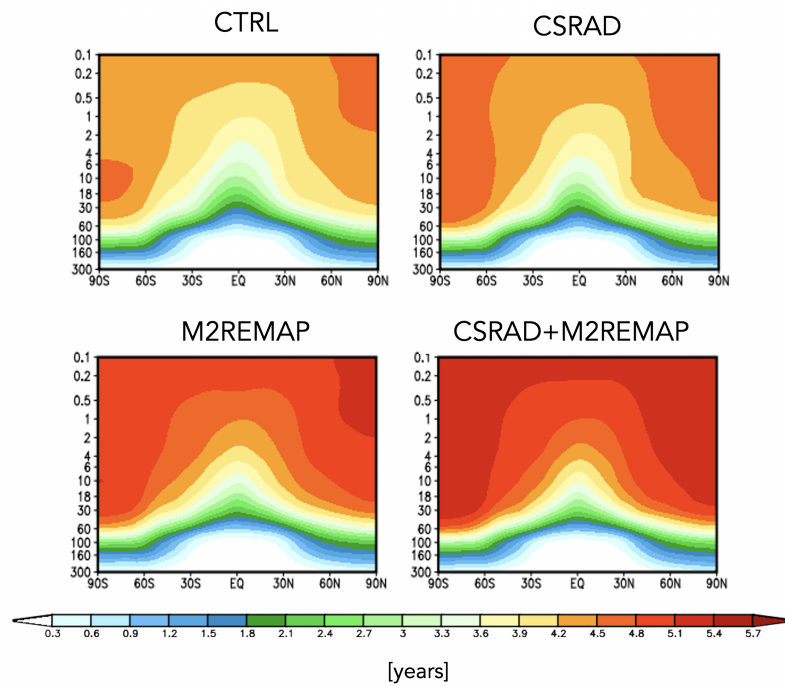


Figure 6. Colors show the simulated 2000-2010 climatological annual mean distributions of the mean age-of-air (Γ) for the CTRL (top left; Table 1, row 1), CSRAD (top right; Table 1, row 2), M2REMAP (bottom left; Table 1, row 3) and combined CSRAD+M2REMAP (bottom right; Table 1, row 4) experiments.

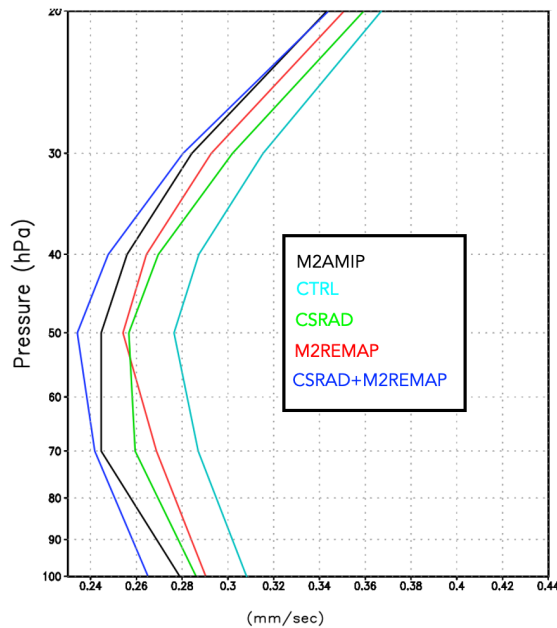
DJF Climatological Mean Tropical Upwelling (w^*)

Figure 7. The DJF 1985-2015 climatological mean vertical residual mean velocity, w^* , averaged between the turnaround latitudes for the CTRL (cyan line; Table 2, row 1), CSRAD (green line; Table 2, row 2), M2REMAP (red line; Table 2, row 3) and combined CSRAD+M2REMAP (blue line; Table 2, row 4) experiments. M2AMIP is shown in black.

504 used in MERRA-2 and in current FV3 core configurations, we now investigate further
 505 the sensitivity of the transport circulation to the choice of remapping interpolation scheme.
 506 In particular, we compare simulations in which total energy is calculated at new mid-
 507 layer pressures using cubic, quadratic and linear interpolation prior to the aposterior in-
 508 tegral conservation (Table 2, rows 5-7). In addition, in this section we seek to understand
 509 how the changes in the Eliassen-Palm flux convergence over NH midlatitudes arise via
 510 analysis of the large-scale wind structure.

511 Figure 8 (left panel) shows a clear sensitivity in tropical upwelling to the choice of
 512 interpolation scheme, with w^* progressively increasing in strength moving from the CU-
 513 BIC to QUADRATIC to LINEAR schemes. This sensitivity is robust across horizontal
 514 resolutions as the same suite of experiments performed at C360 exhibit the same sensi-
 515 tivity (Fig. 8, right panel). While no current model version actually employs a linear
 516 scheme, this suite of experiments highlights the strong sensitivity to choice of interpo-
 517 lation scheme within the remapping algorithm; to the best of our knowledge, this result
 518 has not been reported in the literature. Furthermore, as we show next, this clean set of
 519 experiments allow us to inquire mechanistically into the processes that are driving the
 520 changes in wave convergence over midlatitudes, unencumbered by differences in horizon-
 521 tal resolution, physics, etc.

522 Consistent with our expectations based on the analysis of the previous experiments,
 523 the drivers of the changes in w^* are related to increased wave convergence moving from
 524 the CUBIC to QUADRATIC to LINEAR schemes (Figure 9). Over extratropical lat-
 525 itudes, the zonal force associated with this enhanced wave convergence is associated with
 526 enhanced downwelling at high latitudes that, through mass balance, is accompanied by
 527 enhanced upwelling in the tropics. This indirect impact of higher latitude wave drag is

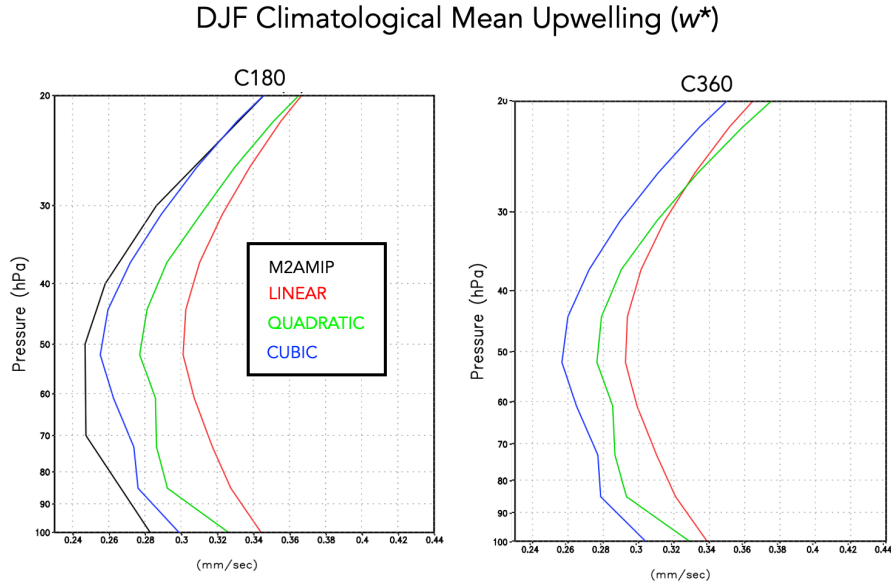


Figure 8. The DJF 1985-2015 climatological mean vertical residual mean velocity, w^* , averaged between the turnaround latitudes for the LINEAR (red line; Table 2, row 5), QUADRATIC (green line; Table 2, row 6) and CUBIC (blue line; Table 2, row 7) experiments. M2AMIP is shown in black. Results from C180 and C360 EMIP experiments are shown in the left and right panels, respectively.

528 evident in Appendix Figure C1, which shows stronger upwelling/downwelling in the LIN-
 529 EAR and QUADRATIC experiments over the tropics/polar region.

530 Next we exploit the fact that these experiments only differ with respect to the in-
 531 terpolation scheme in order to inquire further into the drivers of the wave convergence
 532 changes. To this end, Figure 10 compares profiles of the zonal mean zonal wind between
 533 the CUBIC, QUADRATIC and LINEAR experiments, averaged over the region of en-
 534 hanced wave convergence (i.e. 20°N-60°N). The experiments featuring stronger wave con-
 535 vergence (LINEAR and QUADRATIC) are also simulations with stronger zonal winds,
 536 relative to MERRA-2, especially above 70 hPa. This change in winds occurs at both C180
 537 (Fig. 10, left panel) and C360 (Fig. 10, right panel) resolutions.

538 Structurally, the increase in zonal wind strength over northern extratropical mid-
 539 latitudes is reflective of a poleward shift in the zonal winds as the critical latitude, i.e.
 540 where the zonal wind is zero, shifts northward in the QUADRATIC and, especially, LIN-
 541 EAR integrations, relative to the CUBIC experiment (Figure 11). Since stationary waves
 542 only propagate in westerly zonal flow, the latitude where zonal flow is zero acts a bound-
 543 ary for wave propagation (Hardiman et al. (2014)). As a result, this shift in critical lat-
 544 itude results in enhanced wave propagation and convergence over middle and high lat-
 545 itudes.

546 Figures 10 and 11 highlight how the changes in zonal winds in the LINEAR and
 547 QUADRATIC experiments reflect a degradation in model skill, relative to MERRA-2,
 548 throughout the entire stratosphere. The changes in upwelling, mean age, chemical trace
 549 gases and zonal winds thus provide a coherent and self-consistent picture suggestive of
 550 a degradation in the representation of the stratospheric circulation since MERRA-2. That
 551 is, an increased bias in the stratospheric northern zonal winds are, via their influence on

DJF Climatological Mean Eliassen-Palm Flux Divergence ($\nabla \cdot \mathbf{F}$)

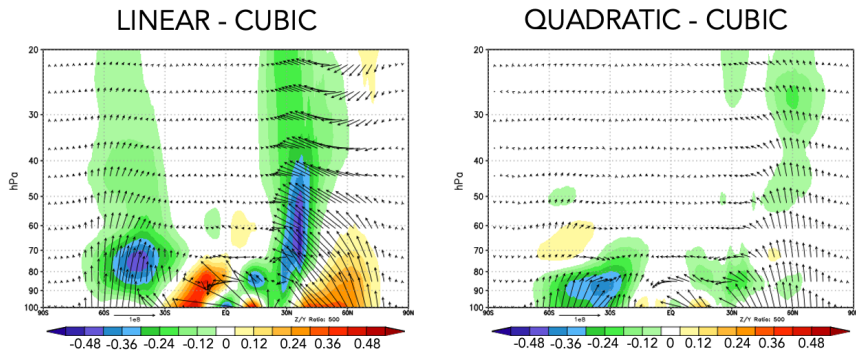


Figure 9. Colors shown anomalies in the DJF 1985-2015 climatological mean Eliassen-Palm (EP) flux divergence in the LINEAR (left) and QUADRATIC (right) experiments, relative to the CUBIC model experiment. Arrows denote anomalies in the vertical and meridional EP flux vectors.

DJF Climatological Mean Zonal Wind (20°N-60°N)

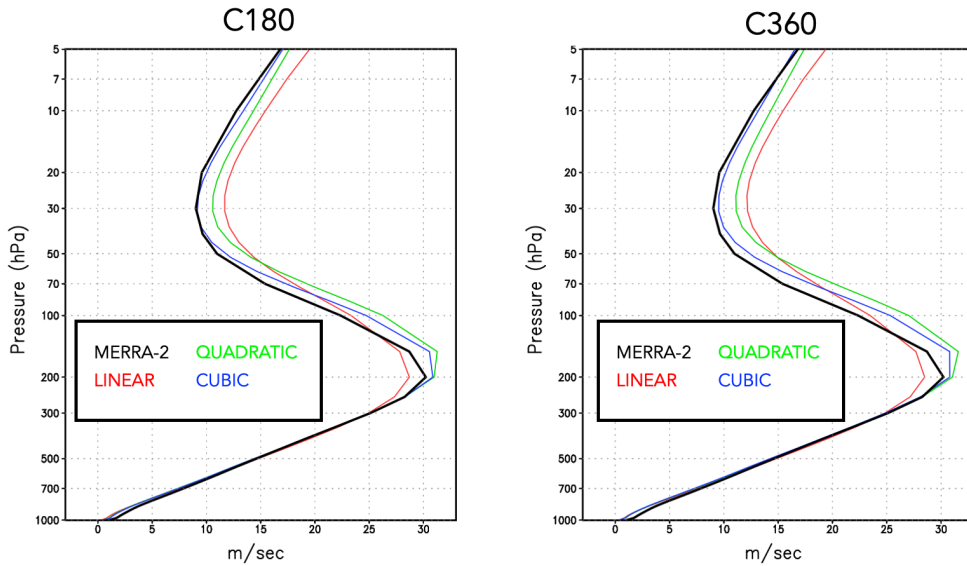


Figure 10. Vertical profiles of the DJF 1985-2015 climatological mean zonal mean zonal winds in the LINEAR (red), QUADRATIC (green) and CUBIC (blue) experiments, averaged between 20°N and 60°N. MERRA-2 is shown in the black line. Results for both C180 (left) and C360 (right) experiments are shown.

DJF Climatological Zonal Mean Zonal Wind Anomalies Relative to MERRA-2

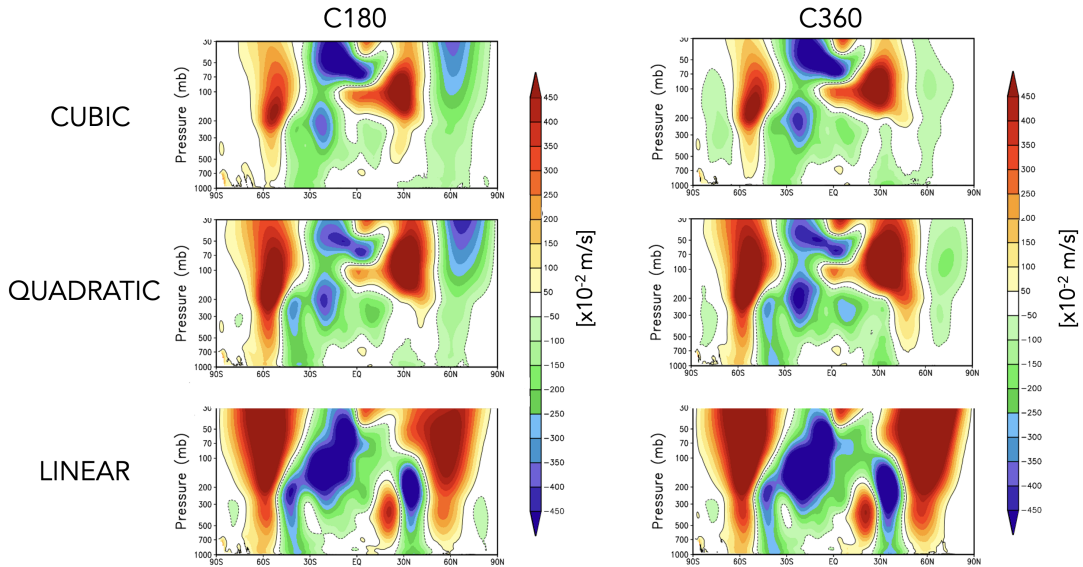


Figure 11. Colors shown anomalies in the DJF 1985-2015 climatological mean zonal mean zonal winds in the CUBIC (top), QUADRATIC (middle) and LINEAR (bottom) experiments, relative to MERRA-2. Results for both C180 (left) and C360 (right) experiments are shown.

552 wave convergence, compromising changes in the strength of the mean meridional over-
 553 turning circulation and its impact on composition. It is interesting to note that the wind
 554 biases also extend into the troposphere and show degraded skill relative to MERRA-2
 555 in the LINEAR and QUADRATIC experiments (Figure 11). Examination of other fields
 556 (i.e. tropopause biases, Appendix Figure D1) present somewhat more of a nuanced story
 557 that depends more sensitively on latitude and season considered. The improvements in
 558 the zonal winds, however, are most relevant for setting the upwelling characteristics within
 559 the tropical lower stratosphere via their influence on wave propagation into that region.

560 Finally, to better understand why these impacts on the winds have such a conse-
 561 quence for the wave convergence properties within the stratosphere, next we examine the
 562 zonal structure of these biases in the middle stratosphere (Figure 12). This reveals that
 563 the enhanced winds in the LINEAR (and, to a lesser extent, QUADRATIC) integrations
 564 are concentrated over the North Pacific at both C180 (Fig. 12, left) and C360 (Fig. 12,
 565 right) resolutions (a similar picture emerges within the troposphere, not shown). As this
 566 region is the primary region dominating the stationary component of the upward flux
 567 of vertical wave activity (Plumb (1985), see their Figure 4) it is perhaps not surprising
 568 that this region is having a profound impact on the mean overturning circulation. Again,
 569 as with the zonal mean wind changes, the increases in wind strength over the North Pa-
 570 cific represent degraded model skill relative to MERRA-2. Note that comparisons with
 571 ERA-5 reveal a similar bias (not shown).

572 4 Conclusions

573 Here we have performed an analysis aimed at understanding differences in the rep-
 574 resentation of the stratospheric circulation in recent candidate systems for GEOS-R21C,
 575 relative to older versions of GEOS similar to the model used to produce MERRA-2. Us-

DJF Climatological 30 hPa Zonal Wind Anomalies Relative to MERRA-2

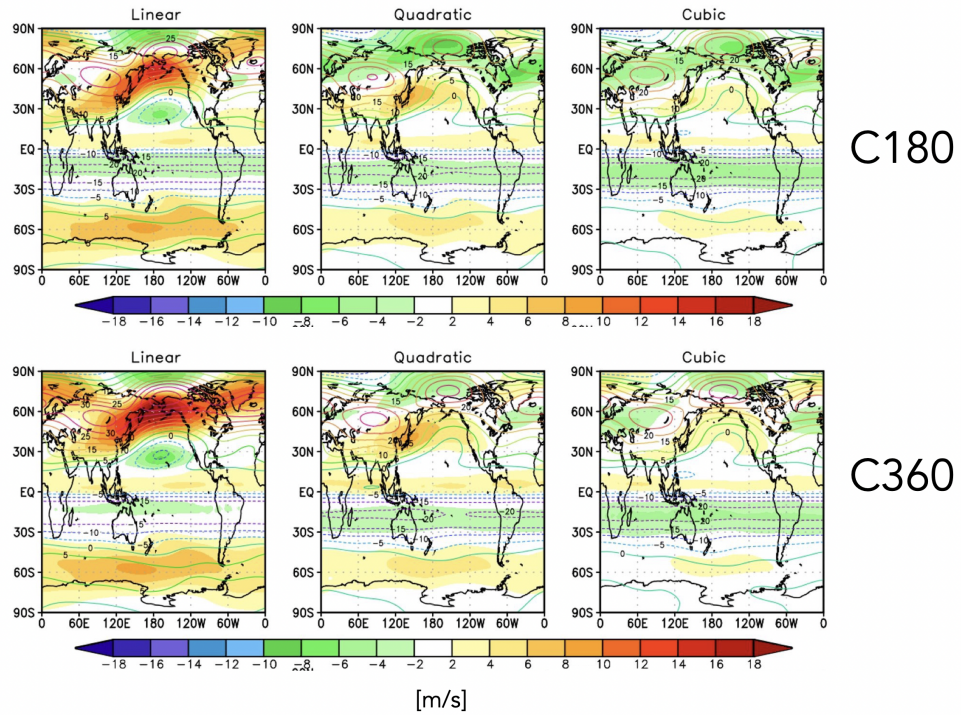


Figure 12. Colors shown anomalies in the DJF 1985-2015 climatological mean zonal winds at 30 hPa in the CUBIC (right), QUADRATIC (middle) and LINEAR (left) experiments, relative to MERRA-2. Results for both C180 (top) and C360 (bottom) experiments are shown.

576 ing targeted experiments oriented at disentangling various model development updates,
 577 we have identified a key role played by changes in the remapping algorithm within the
 578 model’s finite-volume dynamical core. Our key results are as follows:

579 #1. The stratospheric mean age-of-air in GEOS is sensitive to the degree of the
 580 interpolation scheme that is used to calculate layer-mean values of total energy, U, V and
 581 tracers. Different treatment of the vertical remapping algorithm result in mid-stratospheric
 582 (50 hPa) age-of-air differences of ~ 1 year over high latitudes, or about 30% climatolog-
 583 ical mean values.

584 #2. The age-of-air sensitivities reflect, to first order, changes in the strength of trop-
 585 ical upwelling associated with the Brewer-Dobson circulation which are in turn are driven
 586 by changes in EP flux convergence over northern midlatitudes. Changes in wave conver-
 587 gence reflect shifts in (critical lines of) wave propagation that originate in the troposphere
 588 over the Pacific Ocean, a region of strong upward wave activity.

589 #3. The degradation of upwelling statistics manifest in AMIPs, also translate to
 590 degradations in DAS configurations of GEOS.

591 Although our focus here has been on the stratospheric transport circulation, moti-
 592 vating our use of tracer-independent metrics like the age-of-air, our results have clear
 593 implications for constituent transport in the next reanalysis that is currently under de-
 594 velopment (GEOS-R21C). In particular, we showed that the increased age-of-air biases
 595 correspond to increased biases in the representations of CH_4 and N_2O moving from the

596 CCM1 Phase 1 to Phase 2 model configuration. This comports with well-known corre-
 597 lations between the mean age and stratospheric trace gases, reinforcing the fact that model
 598 transport inaccuracies continue to significantly affect simulations of important long-lived
 599 chemical species in the stratosphere (Hall et al. (1999)).

600 Our results highlight the key role played by model numerics in transport (e.g., Rood
 601 (1987)). The sensitivities in the age-of-air documented herein are also consistent in spirit
 602 with the findings in Gupta et al. (2020) who showed significant age differences occurring
 603 between spectral versus finite-volume numerics. Our results, however, suggest that there
 604 remain large sensitivities even within a given (FV) dynamical core. Furthermore, we also
 605 briefly show that statistics derived from long AMIPs also manifest within a data
 606 assimilation context, which raises important questions as to the degree to which model
 607 biases can be ameliorated through assimilation of observations.

608 Looking forward, our findings support and build on the recommendation proposed
 609 in Gupta et al. (2020) for the construction of dynamical core benchmark tests aimed at
 610 determining how underlying AGCM numerics impact climatological transport proper-
 611 ties. In particular, in addition to the age-of-air, the authors propose a range of strato-
 612 spheric circulation diagnostics that should be evaluated including the zonal mean zonal
 613 winds, eddy temperature variance and zonal spectra of eddy kinetic energy. Our anal-
 614 ysis reveals an important role to be played by the climatological zonal mean wind struc-
 615 ture as it impacts wave convergence over midlatitudes; we therefore also recommend ex-
 616 plicit consideration of the Eliassen Palm flux convergence and tropical upwelling (w^*)
 617 fields as they may be crucial for interpreting age-of-air changes.

618 One somewhat incidental – but practical - result from our analysis is that the statis-
 619 tics of $\nabla \cdot \mathbf{F}$ and w^* are well approximated by ensembles of so-called EMIP integrations.
 620 As these are substantially easier to run than AMIPs these could provide a “first pass”
 621 when evaluating new proposed model development changes, without the immediate need
 622 to integrate AMIP-style experiments. We emphasize, however, that this statement should
 623 only apply to a first stage in model development as the age-of-air will reflect the time
 624 integrated impacts of both advection and mixing.

625 Finally, we conclude by noting that, while we have focused on sensitivities within
 626 the FV remapping algorithm, our results have highlighted important sensitivities to changes
 627 in radiation and, to a lesser extent, changes in parameterized convection. Though not
 628 the dominant drivers of the age-of-air changes identified here, the former could poten-
 629 tially influence the age both directly through changes in thermal structure and indirectly
 630 by modifying wave propagation and/or generation in the troposphere. Future work will
 631 focus on examining these impacts.

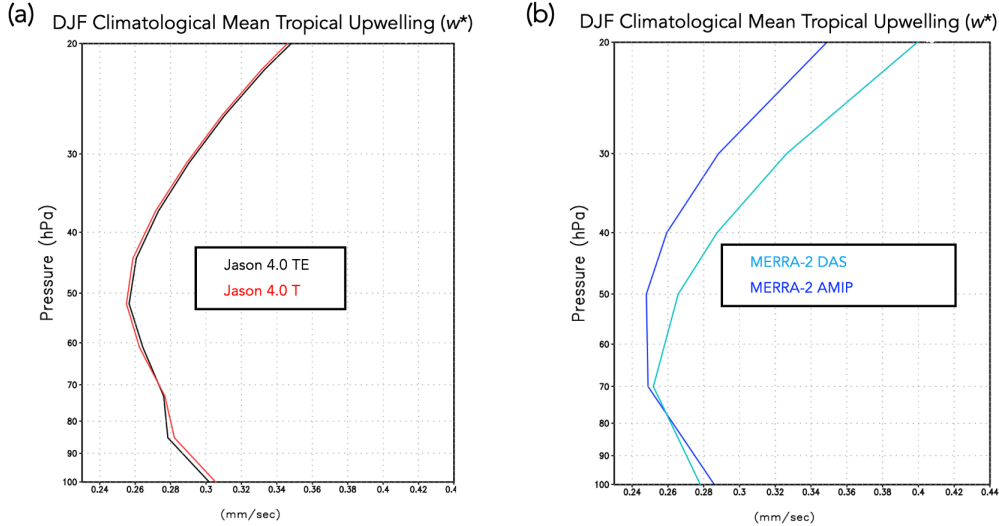


Figure A1. The DJF 1985-2015 climatological mean vertical residual mean velocity, w^* , averaged between the turnaround latitudes compared between two Jason 4.0 experiments remapping to temperature (T) (red) versus total energy (TE) (black) (a) and between MERRA-2 DAS (cyan) and the M2AMIP ensemble (blue) (b).

632 Appendix A Sensitivities in Calculation of TEM Upwelling

633 There are various aspects of the calculation of the TEM circulation that warrant
 634 further comment. First, whereas the modeling experiments listed in Table 2 (rows 5-7)
 635 focus on the sensitivity of Step 5 within the GMAO FV core remapping algorithm to the
 636 choice of interpolation scheme, another difference between the GMAO and FV3 core remap-
 637 ping approaches is the use of TE versus T, respectively. To test the impact of this dif-
 638 ference, we ran a new experiment which is identical to the CUBIC experiment (Table
 639 2, row 7), except that T is remapped from input layer mean pressure locations to stan-
 640 dard output layer mean locations directly using cubic interpolation (i.e., no computa-
 641 tion of TE or a-posteriori energy conservation applied). Appendix Figure A1a shows that
 642 this has little impact on the strength of tropical upwelling, suggesting that the w^* dif-
 643 ferences associated with changes in the remapping algorithm are dominated by sensitiv-
 644 ities to the choice of interpolation scheme, not the use of TE versus T.

645 Second, the vertical component of the TEM circulation (w^*) shows some differences
 646 in vertical structure between MERRA-2 and the 30-member M2AMIP ensemble (Ap-
 647 pendix Figure A1b). This difference in vertical structure appears to reflect a difference
 648 between DAS and free-running configurations of the model, since both DAS configura-
 649 tions shown in Figure 2b share a similar vertical structure. Given this difference, we en-
 650 sure as apples-to-apples a comparison of simulated TEM velocities by comparing all AMIP
 651 results to other AMIPS, and vice versa for the few selected DAS results.

652 Appendix B Correspondence between EMIP and AMIP Upwelling

653 Appendix Figure B1 shows the close correspondence in DJF climatological mean
 654 w^* , averaged between the turnaround latitudes, from AMIP and EMIP experiments us-
 655 ing the same model configuration. This good agreement in upwelling is used to justify
 656 the analysis of the EMIP experiments listed in Table 2 (rows 5-7).

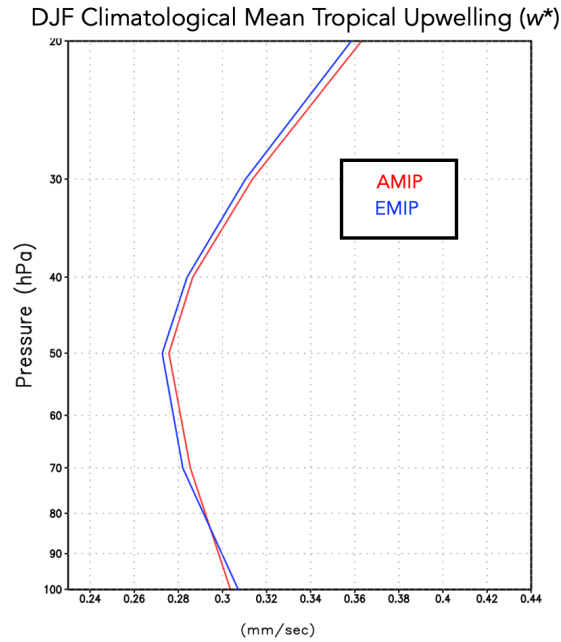


Figure B1. The DJF 1985-2015 climatological mean vertical residual mean velocity, w^* , averaged between the turnaround latitudes for the CTRL experiment (Table 2, row 1). Results based on a 30-year-long AMIP experiment (red line) and a 30-member ensemble of three-month-long EMIP experiments (blue line) are shown.

657

Appendix C Changes in Tropical and High Latitude Upwelling

658

659

660

661

662

663

Appendix Figure C1 compares the behavior in residual mean upwelling among the LINEAR, QUADRATIC and CUBIC experiments over the latitudes between the (tropical) turnaround latitudes (left) and poleward of the northern turnaround latitude (right). The ordering among experiments in both regions reflects how increases in downwelling at high latitudes are, through mass balance, accompanied by enhanced upwelling in the tropics.

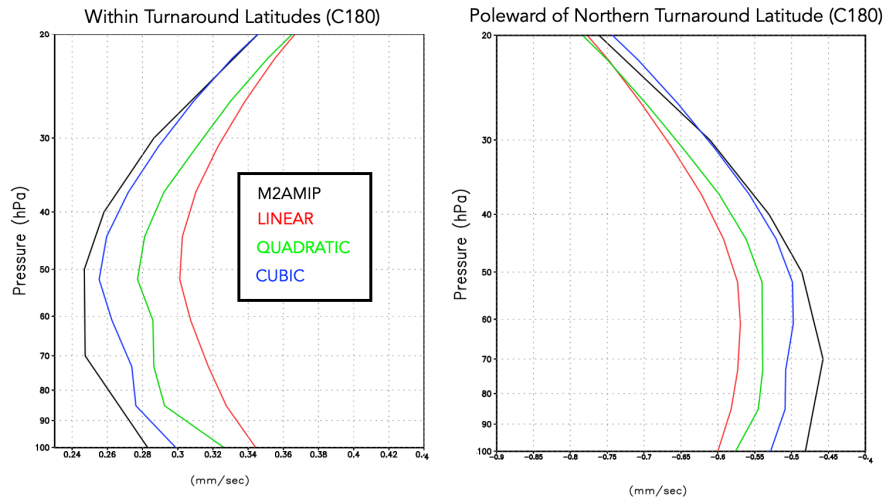
DJF Climatological Mean Upwelling (w^*)

Figure C1. Left: The DJF 1985–2015 climatological mean vertical residual mean velocity, w^* , averaged between the turnaround latitudes for the LINEAR (red line; Table 2, row 5), QUADRATIC (green line; Table 2, row 6) and CUBIC (blue line; Table 2, row 7) experiments. M2AMIP is shown in black. Right: As in left panel, except averaged over latitudes poleward of the northern turnaround latitude. Results in both panels are shown for C180 experiments.

664

Appendix D Tropopause Pressure

665

Appendix Figure D1 compares boreal winter tropopause pressure and temperature among the LINEAR, QUADRATIC and CUBIC experiments, relative to MERRA-2.

666

DJF Climatological Mean Tropopause

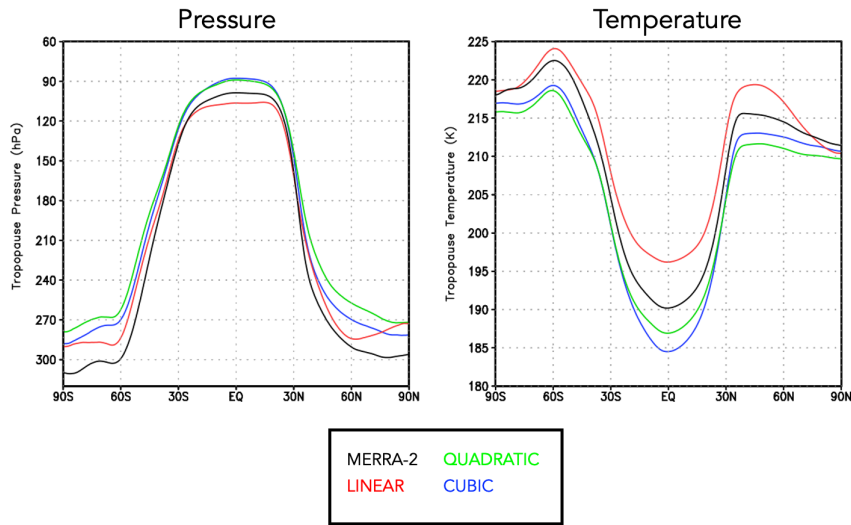


Figure D1. The DJF 1985-2015 climatological mean tropopause pressure (left) and temperature (right) in the CUBIC (blue), QUADRATIC (green) and LINEAR (red) experiments. MERRA-2 is shown in black. Results are shown for the C180 experiments.

667 Acronyms

- 668 **AMIP** Atmospheric Model Intercomparison Project
- 669 **CH₄** methane
- 670 **CCMs** chemistry climate models
- 671 **CCMI** Chemistry Climate Modeling Initiative
- 672 **CCMVal** Chemistry Climate Model Validation
- 673 **CO₂** carbon dioxide
- 674 **CTRL** control
- 675 **CTM** chemistry transport model
- 676 **DAS** Data assimilation
- 677 **DJF** December-January-February
- 678 **EMIP** ensemble AMIP
- 679 **EOS** Earth Observing System
- 680 **EP** Eliassen-Palm
- 681 **FV** finite-volume
- 682 **FP** Forward Processing
- 683 **GEOS** Global Earth Observing System
- 684 **GEOS-R21C** GEOS Retrospective analysis for the 21st Century
- 685 **GMI** Global Modeling Initiative
- 686 **HALOE** Halogen Occultation Experiment
- 687 **MERRA-2** Modern-Era Retrospective Analysis for Research and Applications v2
- 688 **MLS** Microwave Limb Sounder
- 689 **N₂O** nitrous oxide
- 690 **NH** northern hemisphere
- 691 **PPM** piecewise parabolic
- 692 **RRTMG** Rapid Radiative Transfer Model for GCMS

693 **SW** shortwave
 694 **TE** total energy
 695 **TEM** Transformed Eulerian Mean
 696 **UARS** Upper Atmosphere Research Satellite

697 **Open Research Section**

698 TBD

699 **Acknowledgments**

700 C.O. thanks William Putnam and Lawrence Coy for their insight which helped in inter-
 701 preting the results and guiding experimental design. The authors also thank the high-
 702 performance computing resources provided by NASA’s Advanced Supercomputing (NAS)
 703 Division and the NASA Center for Climate Simulation (NCCS) as well as NASA’s Mod-
 704 eling, Analysis and Prediction (MAP) program, which supports the Global Modeling As-
 705 simulation Office and core chemistry-climate and chemistry-modeling activities.

706 **References**

- 707 Abalos, M., Calvo, N., Benito-Barca, S., Garny, H., Hardiman, S. C., Lin, P., ...
 708 others (2021). The Brewer–Dobson circulation in CMIP6. *Atmospheric*
 709 *Chemistry and Physics*, *21*(17), 13571–13591.
- 710 Abalos, M., Orbe, C., Kinnison, D. E., Plummer, D., Oman, L. D., Jöckel, P., ...
 711 others (2020). Future trends in stratosphere-to-troposphere transport in CCM1
 712 models. *Atmospheric Chemistry and Physics*, *20*(11), 6883–6901.
- 713 Abalos, M., Randel, W. J., Kinnison, D. E., & Garcia, R. R. (2017). Using the
 714 artificial tracer e90 to examine present and future UTLS tracer transport in
 715 WACCM. *Journal of the Atmospheric Sciences*, *74*(10), 3383–3403.
- 716 Andrews, D., Holton, J., & Leovy, C. (1987). Middle Atmosphere Dynam-
 717 ics. *Academic Press*, *60*, 489. doi: 10.1175/1520-0469(2003)060<0103:
 718 CEOOAL>2.0.CO;2
- 719 Arnold, N. P., Putman, W. M., & Freitas, S. R. (2020). Impact of resolution and
 720 parameterized convection on the diurnal cycle of precipitation in a global
 721 nonhydrostatic model. *Journal of the Meteorological Society of Japan. Ser. II*.
- 722 Boering, K. A., Wofsy, S., Daube, B., Schneider, H., Loewenstein, M., Podolske, J.,
 723 & Conway, T. (1996). Stratospheric mean ages and transport rates from obser-
 724 vations of carbon dioxide and nitrous oxide. *Science*, *274*(5291), 1340–1343.
- 725 Butchart, N., Cionni, I., Eyring, V., Shepherd, T., Waugh, D., Akiyoshi, H., ...
 726 others (2010). Chemistry–climate model simulations of twenty-first century
 727 stratospheric climate and circulation changes. *Journal of Climate*, *23*(20),
 728 5349–5374.
- 729 Chiodo, G., & Polvani, L. M. (2019). The response of the ozone layer to quadru-
 730 pled CO2 concentrations: Implications for climate. *Journal of Climate*, *32*(22),
 731 7629–7642.
- 732 Chou, M.-D. (1990). Parameterizations for the absorption of solar radiation by O2
 733 and CO2 with application to climate studies. *Journal of Climate*, *3*(2), 209–
 734 217.
- 735 Chou, M.-D. (1992). A solar radiation model for use in climate studies. *Journal of*
 736 *Atmospheric Sciences*, *49*(9), 762–772.
- 737 Chou, M.-D., & Suarez, M. J. (1994). An efficient thermal infrared radiation param-
 738 eterization for use in general circulation models.
- 739 Collow, A. B. M., Mahanama, S. P., Bosilovich, M. G., Koster, R. D., & Schubert,
 740 S. D. (2017). *An evaluation of teleconnections over the united states in an*

- 741 ensemble of AMIP simulations with the MERRA-2 configuration of the GEOS
742 atmospheric model (Tech. Rep.).
- 743 Davis, N. A., Callaghan, P., Simpson, I. R., & Tilmes, S. (2022). Specified dynamics
744 scheme impacts on wave-mean flow dynamics, convection, and tracer transport
745 in CESM2 (WACCM6). *Atmospheric Chemistry and Physics*, *22*(1), 197–214.
- 746 Dietmüller, S., Eichinger, R., Garny, H., Birner, T., Boenisch, H., Pitari, G., ...
747 others (2018). Quantifying the effect of mixing on the mean age of air in
748 CCMVal-2 and CCM1-1 models. *Atmospheric Chemistry and Physics*, *18*(9),
749 6699–6720.
- 750 Eichinger, R., Garny, H., Šácha, P., Danker, J., Dietmüller, S., & Oberländer-Hayn,
751 S. (2020). Effects of missing gravity waves on stratospheric dynamics: Part 1,
752 Climatology. *Climate Dynamics*, *54*(5), 3165–3183.
- 753 Eluszkiewicz, J., Hemler, R. S., Mahlman, J. D., Bruhwiler, L., & Takacs, L. L.
754 (2000). Sensitivity of age-of-air calculations to the choice of advection scheme.
755 *Journal of the Atmospheric Sciences*, *57*(19), 3185–3201.
- 756 Eyring, V., Lamarque, J.-F., Hess, P., Arfeuille, F., Bowman, K., Chipperfield,
757 M. P., ... others (2013). Overview of IGAC/SPARC Chemistry-Climate
758 Model Initiative (CCMI) community simulations in support of upcoming ozone
759 and climate assessments. *SPARC Newsletter*, *40*(January), 48–66.
- 760 Freitas, S. R., Grell, G. A., Molod, A., Thompson, M. A., Putman, W. M., Santos e
761 Silva, C. M., & Souza, E. P. (2018). Assessing the Grell-Freitas convection
762 parameterization in the NASA GEOS modeling system. *Journal of Advances
763 in Modeling Earth Systems*, *10*(6), 1266–1289.
- 764 Freitas, S. R., Putman, W. M., Arnold, N. P., Adams, D. K., & Grell, G. A. (2020).
765 Cascading toward a kilometer-scale GCM: Impacts of a scale-aware convection
766 parameterization in the Goddard Earth Observing System GCM. *Geophysical
767 Research Letters*, *47*(17), e2020GL087682.
- 768 Fujiwara, M., Manney, G. L., Gray, L. J., Wright, J. S., Tegtmeier, S., Ivanciu, I., &
769 Pilch Kedzierski, R. (2022). Sparc reanalysis intercomparison project (s-rip)
770 final report.
- 771 Gelaro, R., McCarty, W., Suárez, M. J., Todling, R., Molod, A., Takacs, L., ...
772 others (2017). The modern-era retrospective analysis for research and applica-
773 tions, version 2 (MERRA-2). *Journal of Climate*, *30*(14), 5419–5454.
- 774 Grell, G. A., & Freitas, S. R. (2014). A scale and aerosol aware stochastic convective
775 parameterization for weather and air quality modeling. *Atmospheric Chemistry
776 and Physics*, *14*(10), 5233–5250.
- 777 Grooß, J.-U., & Russell III, J. M. (2005). A stratospheric climatology for O₃, H₂O,
778 CH₄, NO_x, HCl and HF derived from HALOE measurements. *Atmospheric
779 Chemistry and Physics*, *5*(10), 2797–2807.
- 780 Gupta, A., Gerber, E. P., & Lauritzen, P. H. (2020). Numerical impacts on tracer
781 transport: A proposed intercomparison test of Atmospheric General Circula-
782 tion Models. *Quarterly Journal of the Royal Meteorological Society*, *146*(733),
783 3937–3964.
- 784 Hall, T. M., & Plumb, R. A. (1994). Age as a diagnostic of stratospheric transport.
785 *Journal of Geophysical Research: Atmospheres*, *99*(D1), 1059–1070.
- 786 Hall, T. M., Waugh, D. W., Boering, K. A., & Plumb, R. A. (1999). Evaluation
787 of transport in stratospheric models. *Journal of Geophysical Research: Atmo-
788 spheres*, *104*(D15), 18815–18839.
- 789 Hardiman, S. C., Butchart, N., & Calvo, N. (2014). The morphology of the Brewer-
790 Dobson circulation and its response to climate change in CMIP5 simulations.
791 *Quarterly Journal of the Royal Meteorological Society*, *140*(683), 1958–1965.
- 792 Haynes, P., McIntyre, M., Shepherd, T., Marks, C., & Shine, K. P. (1991). On the
793 “downward control” of extratropical diabatic circulations by eddy-induced
794 mean zonal forces. *Journal of the Atmospheric Sciences*, *48*(4), 651–678.
- 795 Hegglin, M. I., Brunner, D., Peter, T., Hoor, P., Fischer, H., Staehelin, J., ... Weers,

- 796 U. (2006). Measurements of NO, NO_y, N₂O, and O₃ during SPURT: implica-
 797 tions for transport and chemistry in the lowermost stratosphere. *Atmospheric*
 798 *Chemistry and Physics*, 6(5), 1331–1350.
- 799 Holton, J. R., Haynes, P. H., McIntyre, M. E., Douglass, A. R., Rood, R. B., & Pfister,
 800 L. (1995). Stratosphere-troposphere exchange. *Reviews of Geophysics*,
 801 33(4), 403–439.
- 802 Holzer, M., & Hall, T. M. (2000). Transit-time and tracer-age distributions in geo-
 803 physical flows. *Journal of the atmospheric sciences*, 57(21), 3539–3558.
- 804 Iacono, M. J., Delamere, J. S., Mlawer, E. J., Shephard, M. W., Clough, S. A., &
 805 Collins, W. D. (2008). Radiative forcing by long-lived greenhouse gases: Cal-
 806 culations with the AER radiative transfer models. *Journal of Geophysical*
 807 *Research: Atmospheres*, 113(D13).
- 808 Ivy, D. J., Solomon, S., Calvo, N., & Thompson, D. W. (2017). Observed connec-
 809 tions of arctic stratospheric ozone extremes to Northern Hemisphere surface
 810 climate. *Environmental Research Letters*, 12(2), 024004.
- 811 Kouatchou, J., Molod, A., Nielsen, J., Auer, B., Putman, W., & Clune, T. (2015).
 812 *GEOS-5 chemistry transport model user’s guide* (Tech. Rep.).
- 813 Legras, B., Pissot, I., Berthet, G., & Lefèvre, F. (2004). Variability of the lagrangian
 814 turbulent diffusivity in the lower stratosphere. *Atmospheric Chemistry and*
 815 *Physics Discussions*, 4(6), 8285–8325.
- 816 Lin, S.-J. (2004). A “vertically lagrangian” finite-volume dynamical core for global
 817 models. *Monthly Weather Review*, 132(10), 2293–2307.
- 818 Lin, S.-J., Putman, W., & Harris, L. (2017). *The gfdl finite-volume cubed-sphere dy-*
 819 *namical core*. NWS/NCEP/EMC.
- 820 Molod, A., Takacs, L., Suarez, M., & Bacmeister, J. (2015). Development of the
 821 GEOS-5 atmospheric general circulation model: Evolution from MERRA to
 822 MERRA2. *Geoscientific Model Development*, 8(5), 1339–1356.
- 823 Monge-Sanz, B., Chipperfield, M., Simmons, A., & Uppala, S. (2007). Mean age of
 824 air and transport in a CTM: Comparison of different ECMWF analyses. *Geo-*
 825 *physical Research Letters*, 34(4).
- 826 Monge-Sanz, B. M., Bozzo, A., Byrne, N., Chipperfield, M. P., Diamantakis, M.,
 827 Flemming, J., ... others (2022). A stratospheric prognostic ozone for seam-
 828 less Earth system models: performance, impacts and future. *Atmospheric*
 829 *Chemistry and Physics*, 22(7), 4277–4302.
- 830 Morgenstern, O., & Carver, G. D. (2001). Comparison of cross-tropopause transport
 831 and ozone in the upper troposphere and lower stratosphere region. *Journal of*
 832 *Geophysical Research: Atmospheres*, 106(D10), 10205–10221.
- 833 Neu, J., Strahan, S., Braesicke, P., Douglass, A., Huck, P., Oman, L., ... Tegtmeier,
 834 S. (2010). SPARC CCMVal (2010), SPARC Report on the Evaluation of
 835 Chemistry-Climate Models: Chapter 5: Transport. SPARC.
- 836 Neu, J. L., & Plumb, R. A. (1999). Age of air in a “leaky pipe” model of strato-
 837 spheric transport. *Journal of Geophysical Research: Atmospheres*, 104(D16),
 838 19243–19255.
- 839 Oehrlein, J., Chiodo, G., & Polvani, L. M. (2020). The effect of interactive ozone
 840 chemistry on weak and strong stratospheric polar vortex events. *Atmospheric*
 841 *Chemistry and Physics*, 20(17), 10531–10544.
- 842 Orbe, C., Oman, L. D., Strahan, S. E., Waugh, D. W., Pawson, S., Takacs, L. L., &
 843 Molod, A. M. (2017). Large-scale atmospheric transport in GEOS replay simu-
 844 lations. *Journal of Advances in Modeling Earth Systems*, 9(7), 2545–2560.
- 845 Orbe, C., Rind, D., Jonas, J., Nazarenko, L., Faluvegi, G., Murray, L. T., ... oth-
 846 ers (2020). GISS Model E2.2: A climate model optimized for the middle
 847 atmosphere—2. Validation of large-scale transport and evaluation of cli-
 848 mate response. *Journal of Geophysical Research: Atmospheres*, 125(24),
 849 e2020JD033151.
- 850 Orbe, C., Yang, H., Waugh, D. W., Zeng, G., Morgenstern, O., Kinnison, D. E., ...

- 851 others (2018). Large-scale tropospheric transport in the Chemistry–Climate
 852 Model Initiative (CCMI) simulations. *Atmospheric Chemistry and Physics*,
 853 *18*(10), 7217–7235.
- 854 Pan, L. L., Wei, J., Kinnison, D., Garcia, R., Wuebbles, D., & Brasseur, G. P.
 855 (2007). A set of diagnostics for evaluating chemistry-climate models in the ex-
 856 tratropical tropopause region. *Journal of Geophysical Research: Atmospheres*,
 857 *112*(D9).
- 858 Pawson, S., Stajner, I., Kawa, S. R., Hayashi, H., Tan, W.-W., Nielsen, J. E., ...
 859 Livesey, N. J. (2007). Stratospheric transport using 6-h-averaged winds from
 860 a data assimilation system. *Journal of Geophysical Research: Atmospheres*,
 861 *112*(D23).
- 862 Plumb, R. A. (1985). On the three-dimensional propagation of stationary waves.
 863 *Journal of Atmospheric Sciences*, *42*(3), 217–229.
- 864 Plumb, R. A. (1996). A “tropical pipe” model of stratospheric transport. *Journal of*
 865 *Geophysical Research: Atmospheres*, *101*(D2), 3957–3972.
- 866 Plumb, R. A. (2002). Stratospheric transport. *Journal of the Meteorological Society*
 867 *of Japan. Ser. II*, *80*(4B), 793–809.
- 868 Polvani, L. M., Waugh, D. W., Correa, G. J., & Son, S.-W. (2011). Stratospheric
 869 ozone depletion: The main driver of twentieth-century atmospheric circulation
 870 changes in the southern hemisphere. *Journal of Climate*, *24*(3), 795–812.
- 871 Prather, M. J., Zhu, X., Tang, Q., Hsu, J., & Neu, J. L. (2011). An atmospheric
 872 chemist in search of the tropopause. *Journal of Geophysical Research: Atmo-*
 873 *spheres*, *116*(D4).
- 874 Rood, R. B. (1987). Numerical advection algorithms and their role in atmospheric
 875 transport and chemistry models. *Reviews of geophysics*, *25*(1), 71–100.
- 876 Rosenlof, K. H. (1995). Seasonal cycle of the residual mean meridional circulation
 877 in the stratosphere. *Journal of Geophysical Research: Atmospheres*, *100*(D3),
 878 5173–5191.
- 879 Son, S.-W., Tandon, N. F., Polvani, L. M., & Waugh, D. W. (2009). Ozone hole and
 880 Southern Hemisphere climate change. *Geophysical Research Letters*, *36*(15).
- 881 Strahan, S., Douglass, A., & Newman, P. (2013). The contributions of chemistry
 882 and transport to low arctic ozone in March 2011 derived from aura MLS obser-
 883 vations. *Journal of Geophysical Research: Atmospheres*, *118*(3), 1563–1576.
- 884 Thiele, G., & Sarmiento, J. (1990). Tracer dating and ocean ventilation. *Journal of*
 885 *Geophysical Research: Oceans*, *95*(C6), 9377–9391.
- 886 Waugh, D., & Hall, T. (2002). Age of stratospheric air: Theory, observations, and
 887 models. *Reviews of Geophysics*, *40*(4), 1–1.
- 888 Weaver, C. J., Douglass, A. R., & Rood, R. B. (1993). Thermodynamic balance
 889 of three-dimensional stratospheric winds derived from a data assimilation
 890 procedure. *Journal of Atmospheric Sciences*, *50*(17), 2987–2993.